The Astrophysical Journal Letters, 789:L20 (6pp), 2014 July 1 doi:10.1088/2041-8205/789/1/L20

THE ALBEDOS OF *KEPLER*'S CLOSE-IN SUPER-EARTHS

Brice-Olivier Demory[1,2]
[1] Astrophysics Group, Cavendish Laboratory, J.J. Thomson Avenue, Cambridge CB3 0HE, UK; bod21@cam.ac.uk
[2] Department of Earth, Atmospheric, and Planetary Sciences, Massachusetts Institute of Technology, 77 Massachusetts Avenue, Cambridge, MA 02139, USA
Received 2013 December 12; accepted 2014 May 3; published 2014 June 19

ABSTRACT

Exoplanet research focusing on the characterization of super-Earths is currently limited to the handful of targets orbiting bright stars that are amenable to detailed study. This Letter proposes to look at alternative avenues to probe the surface and atmospheric properties of this category of planets, known to be ubiquitous in our galaxy. I conduct Markov Chain Monte Carlo light-curves analyses for 97 *Kepler* close-in $R_P \lesssim 2.0\ R_\oplus$ super-Earth candidates with the aim of detecting their occultations at visible wavelengths. Brightness temperatures and geometric albedos in the *Kepler* bandpass are constrained for 27 super-Earth candidates. A hierarchical Bayesian modeling approach is then employed to characterize the population-level reflective properties of these close-in super-Earths. I find median geometric albedos A_g in the *Kepler* bandpass ranging between 0.16 and 0.30, once decontaminated from thermal emission. These super-Earth geometric albedos are statistically larger than for hot Jupiters, which have medians A_g ranging between 0.06 and 0.11. A subset of objects, including Kepler-10b, exhibit significantly larger albedos ($A_g \gtrsim 0.4$). I argue that a better understanding of the incidence of stellar irradiation on planetary surface and atmospheric processes is key to explain the diversity in albedos observed for close-in super-Earths.

Key words: planetary systems – techniques: photometric

Online-only material: color figures

1. INTRODUCTION

Super-Earth mass and radius measurements leave significant degeneracy regarding their bulk composition. Even with an excellent precision on a super-Earth's physical parameters, similar masses and radii could be interpreted very differently (Rogers & Seager 2010; Miller-Ricci & Fortney 2010). One work-around is to have recourse to other types of measurements, such as transmission spectroscopy, occultation, and phase-curve photometry to constrain the atmospheric, and possibly surface properties. All of these techniques, requiring bright ($K < 9$) host stars, have been successfully applied to several hot-Jupiter systems and boosted exoplanet characterization to a level far beyond the mass–radius interpretation alone (e.g., Deming & Seager 2009). To date, however, only three transiting super-earths orbiting bright stars have been detected: GJ1214b (Charbonneau et al. 2009), 55Cnc e (Demory et al. 2011; Winn et al. 2011), and more recently, HD 97658b (Dragomir et al. 2013). All of these super-Earths have mean densities favoring volatile-rich compositions.

Remarkably, *Kepler* has revealed a large population of smaller, close-in hot super-Earths similar to CoRoT-7b (Léger et al. 2009) and Kepler-10b (Batalha et al. 2011). These strongly irradiated rocky planets could potentially harbor minimal atmospheres resulting from ground sublimation. Such atmospheres would be primarily made of monoatomic Na and O, O_2, and SiO (Schaefer & Fegley 2009; Miguel et al. 2011). Close-in super-Earths are expected to be tidally locked to their host stars, resulting in large temperature contrasts between the planet's day side and night side, to the point where the atmosphere would condense out at the day–night terminator (Castan & Menou 2011; Heng & Kopparla 2012).

In this Letter, I propose an approach to explore the reflective properties of close-in super-Earths with no dependence on theoretical models. I conduct a search for occultations over a large sample of super-Earths so as to identify common patterns of their surface and/or atmosphere properties.

This Letter is organized as follows. Section 2 describes the photometric analysis, including data reduction and light-curve modeling. Section 3 presents the hierarchical Bayesian framework used to interpret the data while Section 4 discusses the possible origin of visible flux from *Kepler*'s close-in super-Earths.

2. PHOTOMETRIC ANALYSIS

2.1. Selection of Candidates

The target selection is based on the *Kepler* quarters Q0 through Q13 (see for Q1–Q8 Burke et al. 2014), which represents 3 yr of quasi-continuous monitoring obtained between 2009 May and 2012 June. All Kepler Objects of Interest (KOIs) with radii $R_P < 2.25\ R_\oplus$ are kept. Since this study focuses on how the incident radiation is processed by the planet surface/atmosphere, only those KOI that receive significant irradiation with orbital periods $P < 10$ days are retained. These two selection criteria result in 97 KOIs that are not flagged as false positives on MAST.

2.2. Light-curve Modeling

The Q0–Q13 long-cadence simple aperture photometry (Jenkins et al. 2010) is retrieved from MAST[3] for each of these 97 planet candidates. Instrumental systematics are mitigated by fitting the first four cotrending basis vectors to each quarter using the PyKE software (Still & Barclay 2012). For each quarter, the degree of photometric dilution is estimated by using the contamination factor in the fits file headers. Each quarter is then normalized to the median.

[3] http://archive.stsci.edu/kepler/

The goal of this analysis is to refine the transit parameters and characterize the occultation in the *Kepler* bandpass for each planet candidate. For this purpose, I use the Markov Chain Monte Carlo (MCMC) implementation presented in Gillon et al. (2012). The long cadence 29.9 minute exposure time is taken into account by resampling the photometric time series to one minute cadence directly in the MCMC framework (e.g., Kipping 2010).

I assume a quadratic law for the limb-darkening (LD) and use $c_1 = 2u_1 + u_2$ and $c_2 = u_1 - 2u_2$ as jump parameters, where u_1 and u_2 are the quadratic coefficients. u_1 and u_2 are drawn from the theoretical tables of Claret & Bloemen (2011) for the corresponding $T_{\rm eff}$ and log g values extracted from the Q1–Q16 star properties catalog of Huber et al. (2014). Constraining the stellar density from the transit photometry is more difficult for super-Earths than for hot Jupiters (e.g., Demory & Seager 2011) because of the smaller planet/star radius ratio. I thus include Gaussian priors in the MCMC fit for the stellar radius, $T_{\rm eff}$, and log g values, extracted from Huber et al. (2014).

Each MCMC fit has the following set of jump parameters: the planet/star radius ratio, $R_P/R_\star$, the impact parameter, b, the transit duration from first to fourth contact, T_{14}, the time of minimum light, T_0, the orbital period, P, the occultation depth, $dF_{\rm occ}$, the two LD combinations, c_1 and c_2, and the two parameters, $\sqrt{e}\cos\omega$ and $\sqrt{e}\sin\omega$. I use Gaussian priors for c_1 and c_2, based on the theoretical tables. To improve the MCMC iteration efficiency and because the planet candidates have short orbital periods, I further impose Gaussian priors on $\sqrt{e}\cos\omega$ and $\sqrt{e}\sin\omega$ by centering the distributions on zero and assuming a standard deviation of 0.45 for both parameters. These priors prevent the MCMC fit from exploring high eccentricity configurations that seem highly unlikely for such systems (Hadden & Lithwick 2014). Negative occultation values are allowed in the MCMC fit to avoid biasing occultation posteriors toward positive values.

I divide the photometric time series in ∼24–48 hr segments and fit for each of them the smooth photometric variations due to stellar variability with a time-dependent quadratic polynomial in the MCMC fit. Baseline model coefficients are determined at each step of the MCMC procedure for each light curve using a singular value decomposition method. The resulting coefficients are then used to correct the raw photometric light curves. For each data segment, correlated noise is accounted for, following Gillon et al. (2010), to ensure reliable error bars on the fitted parameters.

One MCMC fit consisting of two Markov chains of 100,000 steps is performed for each planet candidate and their convergence is checked using the Gelman–Rubin statistic criterion (Gelman & Rubin 1992). MCMC fit results for all KOI are shown in Table 1.

2.3. Albedos, Brightness, and Equilibrium Temperatures

The purpose of the present study is to characterize the planetary total emission in the *Kepler* bandpass, which is likely to have both thermal and reflected light components. Thus, the occultation in the *Kepler* bandpass, $dF_{\rm occ,kep}$, alone does not unambiguously provide a direct estimate of the geometric albedo nor the planet's temperature. I therefore define in the following the "total" albedo, as being a direct translation of the full occultation depth into an albedo estimate.

Both the total albedo and brightness temperature are useful means to convert the occultation depth into physical quantities. I use the posterior distributions functions obtained from the MCMC analyses to compute total albedo and brightness temperature values for all planet candidates.

The total albedo in the *Kepler* bandpass is

$$A_t = dF_{\rm occ,kep}\left(\frac{a}{Rp}\right)^2. \quad (1)$$

Assuming a planetary blackbody spectrum, the planetary brightness temperature, T_B, in the *Kepler* bandpass is obtained from the following equation:

$$dF_{\rm occ,kep} = \frac{R_P^2}{R_\star^2}\frac{\int B_\lambda(T_B)\Gamma_\lambda d\lambda}{\int F_\lambda^\star \Gamma_\lambda d\lambda}, \quad (2)$$

where Γ_λ is the *Kepler* transmission function and B_λ is the Planck function. The stellar flux density, $F_\lambda^\star$, is obtained by matching each host's properties (Huber et al. 2014) to the closest MARCS stellar model of Gustafsson et al. (2008).

Several planet candidates that are part of the sample exhibit a moderate photometric signal-to-noise ratio (S/N) and a short transit duration, which, combined with long-cadence time series, prevent us from obtaining a precise estimate of $a/R_\star$ (see also Sanchis-Ojeda et al. 2013). As a consequence, a mediocre precision on both the albedo and equilibrium temperature is derived for these candidates. In a first step, I therefore base the analysis on the brightness temperature instead of the albedo.

2.4. False Positive Assessment and Occultation Detectability

False positives are likely to contaminate the sample. In the radius range considered in this study, it is expected that the corresponding false positive rate ranges from 5% to 15% (Fressin et al. 2013). All obvious false-positives have been withdrawn during the Q1–Q8 (Burke et al. 2014) extensive vetting effort. I choose A_t as a means to discard false positives (e.g., Batalha et al. 2010; Demory & Seager 2011). I keep only those planet candidates that have a total albedo uncertainty less than 1.0. This criterion results in a list of 27 candidates, representing 28% of the initial sample. Keeping candidates with $\sigma_{A_t} < 1.0$ is a conservative approach that eliminates most high-albedo false positives but also low-S/N planet candidates for which no occultation is detected. This selection criterion does not bias the results about non detections, as high-S/N planetary candidates for which no occultation is detected (i.e., low albedo) will have precise uncertainties on their albedos and will therefore be retained. I use a T_B versus period distribution as a means to identify remaining false positives. I find that KOI 2272.01 (see also Ofir & Dreizler 2013), 2545.01 and 2636.01 are likely diluted eclipsing binaries. Among the 27 KOIs resulting from this geometric albedo based selection, only four have periods longer than four days and all have total albedos <1. Radius and orbital period distributions for the selected candidates are shown in Figure 1. As expected, I find that the number of candidates showing an occultation decreases with increasing orbital period, strengthening the planetary nature of the targets (Slawson et al. 2011).

2.5. Individual Super-Earth Brightness Temperatures

Figure 2 shows for each planet candidate the brightness temperature derived from the occultation depth in the *Kepler* bandpass versus the planet's equilibrium temperature, $T_{\rm eq,0} = T_\star\sqrt{(R_\star/2a)}$, assuming a null Bond albedo and an efficient heat recirculation (Hansen 2008). The red line is the maximum

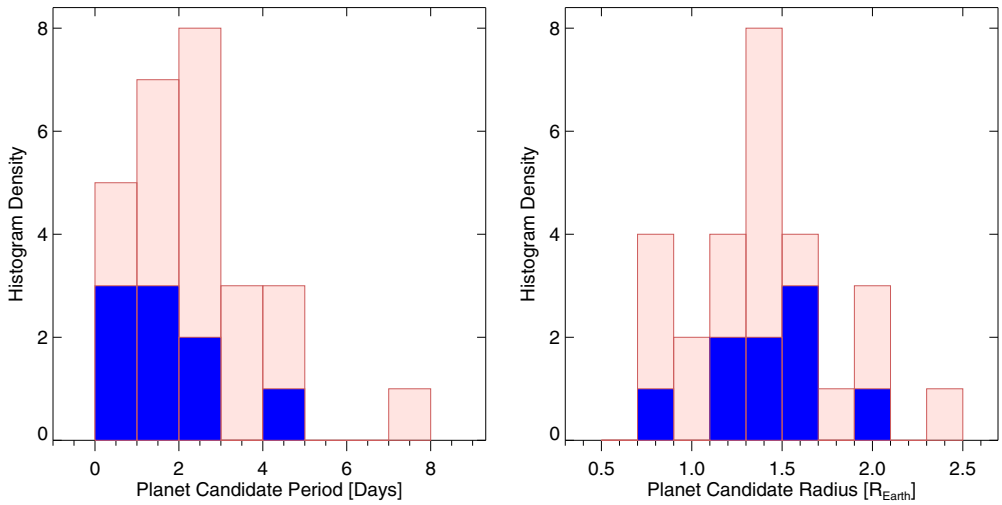

Figure 1. Properties of the selected *Kepler* super-Earth-sized candidates. Left: histogram of orbital periods. Right: histogram of radii. The red bars show the 18 KOIs for which the occultation depth is compatible with 0 at the 1σ level. The blue bars indicate the nine objects that have a determination of their brightness temperature. (A color version of this figure is available in the online journal.)

Table 1
System Parameters, Brightness Temperatures, and Albedos of this Study's Super-Earth Sample

KOI	Period (days)	R_P ($R_\oplus$)	Rp/$R_\star$	a/$R_\star$	$T_{\rm eq,0}$ (K)	Occ. depth (ppm)	T_B (K)	A_t	$A_{g,\rm max}$	$A_{g,\rm min}$
69.01	4.727	$1.51^{+0.07}_{-0.05}$	$0.01564^{+0.00060}_{-0.00042}$	$9.998^{+1.200}_{-1.500}$	1267^{+77}_{-96}	$2.2^{+0.7}_{-0.8}$	2600^{+100}_{-140}	$0.88^{+0.48}_{-0.34}$	0.88	0.87
70.02	3.696	$1.87^{+0.35}_{-0.21}$	$0.01930^{+0.00120}_{-0.00160}$	$8.167^{+3.500}_{-1.900}$	1352^{+291}_{-159}	$-1.6^{+2.4}_{-2.4}$	<2440	<0.43	<0.43	<0.41
72.01	0.837	$1.39^{+0.04}_{-0.03}$	$0.01258^{+0.00020}_{-0.00012}$	$3.468^{+0.150}_{-0.200}$	2136^{+49}_{-63}	$7.4^{+1.1}_{-1.0}$	3270^{+70}_{-70}	$0.56^{+0.09}_{-0.10}$	0.54	0.41
85.02	2.155	$1.43^{+0.08}_{-0.05}$	$0.00956^{+0.00048}_{-0.00026}$	$3.891^{+0.510}_{-0.770}$	2211^{+146}_{-219}	$-0.5^{+0.8}_{-0.9}$	<2720	<0.13	<0.11	<−0.05
167.01	4.920	$2.39^{+1.22}_{-0.29}$	$0.01953^{+0.00040}_{-0.00025}$	$8.559^{+0.530}_{-1.000}$	1569^{+60}_{-106}	$2.1^{+3.7}_{-3.8}$	<2990	<1.11	<1.11	<1.07
262.01	7.813	$2.04^{+0.05}_{-0.05}$	$0.01225^{+0.00014}_{-0.00015}$	$3.306^{+0.120}_{-0.110}$	2420^{+52}_{-49}	$-2.6^{+7.7}_{-3.8}$	<3500	<0.56	<0.52	<0.32
292.01	2.587	$1.43^{+0.28}_{-0.15}$	$0.01414^{+0.00035}_{-0.00064}$	$6.967^{+1.700}_{-0.760}$	1554^{+191}_{-89}	$1.1^{+2.8}_{-2.8}$	<2780	<0.95	<0.94	<0.91
299.01	1.542	$1.48^{+0.20}_{-0.06}$	$0.01592^{+0.00056}_{-0.00030}$	$5.733^{+0.460}_{-0.790}$	1647^{+72}_{-118}	$2.3^{+2.8}_{-2.8}$	<2820	<0.66	<0.65	<0.60
321.01	2.426	$1.31^{+0.23}_{-0.08}$	$0.01280^{+0.00022}_{-0.00043}$	$5.847^{+0.870}_{-0.350}$	1665^{+128}_{-60}	$-0.6^{+1.9}_{-1.9}$	<2700	<0.40	<0.39	<0.34
343.02	2.024	$1.92^{+0.29}_{-0.29}$	$0.01471^{+0.00040}_{-0.00065}$	$4.996^{+1.100}_{-0.540}$	1811^{+202}_{-103}	$3.2^{+2.9}_{-3.0}$	2780^{+260}_{-740}	$0.37^{+0.41}_{-0.34}$	0.36	0.29
665.02	1.612	$1.12^{+0.58}_{-0.14}$	$0.00962^{+0.00045}_{-0.00040}$	$3.253^{+0.620}_{-0.610}$	2395^{+235}_{-236}	$6.2^{+2.6}_{-2.5}$	3560^{+210}_{-280}	$0.71^{+0.52}_{-0.36}$	0.67	0.45
975.01	2.786	$1.53^{+0.02}_{-0.03}$	$0.00784^{+0.00007}_{-0.00011}$	$5.617^{+0.500}_{-0.170}$	1829^{+82}_{-30}	$0.9^{+0.3}_{-0.4}$	2950^{+120}_{-220}	$0.51^{+0.20}_{-0.20}$	0.51	0.43
1128.01	0.975	$1.21^{+0.18}_{-0.09}$	$0.01386^{+0.00029}_{-0.00087}$	$3.495^{+0.900}_{-0.310}$	2075^{+269}_{-101}	$2.2^{+2.6}_{-3.0}$	<2900	<0.30	<0.28	<0.15
1169.01	0.689	$1.26^{+0.30}_{-0.06}$	$0.01304^{+0.00230}_{-0.00044}$	$2.970^{+0.400}_{-1.200}$	2328^{+162}_{-472}	$13.5^{+3.0}_{-3.1}$	3550^{+120}_{-140}	$0.70^{+0.35}_{-0.48}$	0.67	0.48
1824.02	1.678	$1.67^{+1.01}_{-0.37}$	$0.01156^{+0.00064}_{-0.00027}$	$4.804^{+0.610}_{-1.100}$	2025^{+137}_{-240}	$5.3^{+2.2}_{-2.3}$	3370^{+180}_{-280}	$0.92^{+0.58}_{-0.40}$	0.90	0.78
1883.01	2.707	$1.00^{+0.48}_{-0.16}$	$0.00844^{+0.00022}_{-0.00069}$	$3.888^{+2.000}_{-0.660}$	2254^{+582}_{-202}	$-0.7^{+1.3}_{-1.2}$	<2980	<0.28	<0.25	<0.06
1890.01	4.336	$1.58^{+0.08}_{-0.05}$	$0.00970^{+0.00039}_{-0.00021}$	$7.248^{+0.810}_{-1.200}$	1601^{+91}_{-134}	$-0.2^{+1.5}_{-1.4}$	<2880	<0.84	<0.83	<0.79
1929.02	3.293	$1.37^{+0.22}_{-0.30}$	$0.00921^{+0.00034}_{-0.00110}$	$3.117^{+2.000}_{-0.580}$	2276^{+731}_{-215}	$0.5^{+2.3}_{-1.9}$	<3110	<0.33	<0.30	<0.12
1937.01	1.411	$1.21^{+0.14}_{-0.14}$	$0.01842^{+0.00150}_{-0.00066}$	$6.863^{+0.770}_{-1.700}$	1174^{+74}_{-150}	$-0.4^{+3.8}_{-4.0}$	<2220	<0.53	<0.53	<0.52
1961.01	1.908	$1.94^{+1.19}_{-0.82}$	$0.01078^{+0.00039}_{-0.00051}$	$6.352^{+1.400}_{-0.890}$	1553^{+177}_{-115}	$0.8^{+2.3}_{-2.6}$	<2930	<1.08	<1.08	<1.04
1964.01	2.229	$0.74^{+0.13}_{-0.10}$	$0.00710^{+0.00013}_{-0.00047}$	$6.205^{+1.900}_{-0.630}$	1574^{+243}_{-83}	$-0.1^{+0.6}_{-0.7}$	<2610	<0.43	<0.42	<0.39
2049.01	1.569	$1.40^{+0.92}_{-0.16}$	$0.01174^{+0.00073}_{-0.00039}$	$3.617^{+0.570}_{-0.880}$	2358^{+194}_{-300}	$3.8^{+3.4}_{-3.5}$	3190^{+320}_{-870}	$0.36^{+0.43}_{-0.27}$	0.33	0.12
2072.01	1.543	$0.91^{+0.40}_{-0.12}$	$0.01038^{+0.00027}_{-0.00120}$	$2.442^{+1.600}_{-0.390}$	2751^{+903}_{-231}	$1.8^{+4.4}_{-5.2}$	<3450	<0.34	<0.27	<−0.05
2079.01	0.694	$0.83^{+0.31}_{-0.16}$	$0.00681^{+0.00049}_{-0.00059}$	$2.560^{+0.880}_{-0.550}$	2466^{+429}_{-273}	$4.4^{+1.9}_{-2.3}$	3540^{+220}_{-380}	$0.62^{+0.86}_{-0.29}$	0.58	0.34
2332.01	3.701	$1.39^{+1.11}_{-0.75}$	$0.00795^{+0.00033}_{-0.00055}$	$3.682^{+1.200}_{-0.580}$	1985^{+330}_{-167}	$-0.8^{+2.7}_{-3.6}$	<3120	<0.58	<0.56	<0.46
2470.01	2.175	$0.73^{+0.31}_{-0.07}$	$0.00795^{+0.00079}_{-0.00051}$	$3.584^{+0.760}_{-1.100}$	2142^{+234}_{-333}	$0.3^{+3.3}_{-3.1}$	<3370	<0.73	<0.71	<0.56
2492.01	0.985	$0.90^{+0.35}_{-0.11}$	$0.00926^{+0.00061}_{-0.00081}$	$2.658^{+1.100}_{-0.730}$	2628^{+547}_{-368}	$2.1^{+5.0}_{-5.4}$	<3680	<0.58	<0.53	<0.25

Notes. Planet candidates for which the occultation depth is compatible with 0 have their T_B and albedo values shown as 1σ upper limits.

equilibrium temperature, $T_{\rm eq,max}$, with no heat recirculation, while the blue line is for an efficient redistribution, both with a null albedo. The planet candidates that are part of the sample span equilibrium temperatures ranging from 1200 K to 2800 K.

To investigate more precisely how T_B evolves with the equilibrium temperature, I compute $\Delta T = T_B - T_{\rm eq,max}$ for each super-Earth candidate in Figure 3. The red dashed line depicts planets with $T_B = T_{\rm eq,max}$. It is important to note that across the wide range of equilibrium temperatures studied here, the sensitivity to small ΔT is better in the elevated $T_{\rm eq}$ regime than in the lower end. Upper limits on ΔT are obtained for planets in the less populated area of low $T_{\rm eq}$/low ΔT, but no

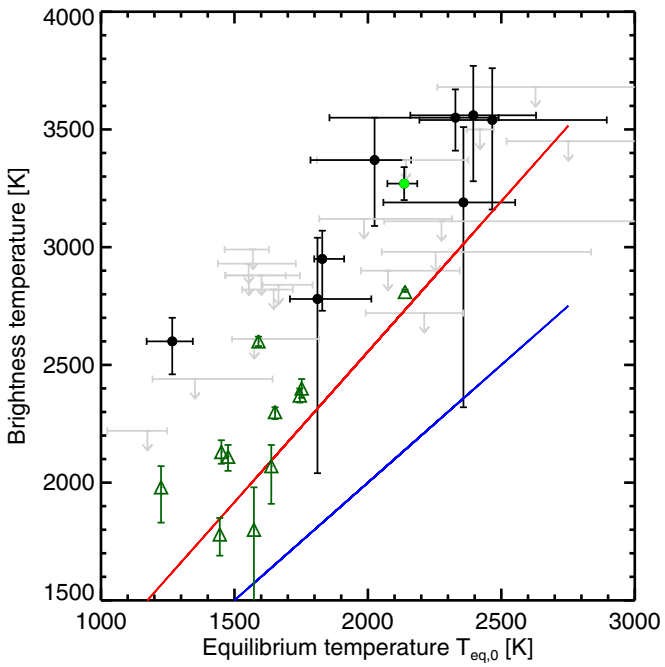

Figure 2. Brightness temperatures of *Kepler* super-Earth-sized candidates. The brightness temperatures measured from the occultation in the *Kepler* bandpass are shown for the 27 selected super-Earth candidates. The red and blue lines depict the equilibrium temperature, assuming null and efficient heat redistribution, respectively, both for a zero Bond Albedo. The green disk shows Kepler-10b and the triangles are the *Kepler* published hot Jupiters (Heng & Demory 2013) that have a constraint on their occultation depth. Planet candidates for which the occultation depth is compatible with 0 at the 1σ level are shown in gray as 1σ upper limits.

(A color version of this figure is available in the online journal.)

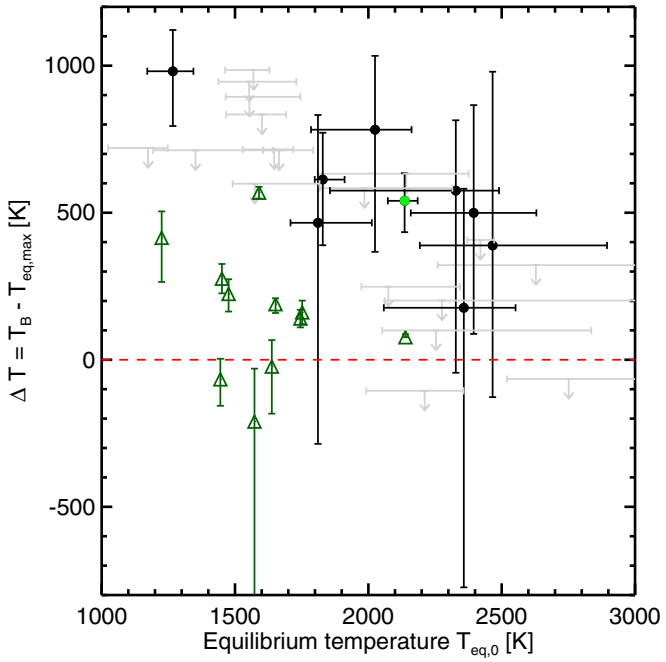

Figure 3. Brightness temperature excesses of *Kepler* super-Earth-sized candidates. The brightness temperature excesses ($\Delta T = T_B - T_{\rm eq,max}$) are shown for the 27 selected planetary candidates as a function of the equilibrium temperature, $T_{\rm eq,0}$. Triangles depict *Kepler* published hot Jupiters (Heng & Demory 2013) that have a constraint on their occultation depth. The green disk represents Kepler-10b. Planet candidates for which the occultation depth is compatible with 0 at the 1σ level are shown in gray as 1σ upper limits.

(A color version of this figure is available in the online journal.)

objects in the high $T_{\rm eq}$/high ΔT are found, where the sensitivity is optimal. I pursue the analysis in a Bayesian framework to explore the incidence of this bias on the results. I find no correlation between the occultation S/N and ΔT (Spearman's rank correlation coefficient of 0.25).

3. CONSTRAINING T_B AND A_g AT THE POPULATION LEVEL USING HIERARCHICAL BAYESIAN MODELING

The data presented in Table 1 include several non-detections and upper limits. I retain them intentionally to avoid biasing the interpretations toward a sub-group of objects that would not be representative of the entire population of planets studied here. Furthermore, the maximum-likelihood estimates alone cannot thoroughly represent the probability intervals of T_B or A_g. I choose an approach based on a hierarchical Bayesian model that follows the method described by Hogg et al. (2010) and Rogers (2014). In summary, I assume a parameterized model for the true distribution of T_B and A_g that are constrained at the population level by the individual planet MCMC posterior probability distributions (PPD). I briefly describe the method and present the results below.

3.1. Methodology

I consider N stars indexed by n. Each star is orbited by one or more planets whose transit and occultation parameters derived from the MCMC, are denoted by $\boldsymbol{\theta_n}$. The *Kepler* photometric time series obtained on each star are denoted by $\boldsymbol{y_n}$. In Section 2 the MCMC procedure computes the PPD for each parameter in $\boldsymbol{\theta_n}$:

$$p(\boldsymbol{\theta_n} \mid \boldsymbol{y_n}) = \frac{1}{Z_n} p(\boldsymbol{y_n} \mid \boldsymbol{\theta_n}) p_0(\boldsymbol{\theta_n}), \quad (3)$$

where Z_n is a normalization constant, $p(\boldsymbol{y_n} \mid \boldsymbol{\theta_n})$ is the likelihood, and $p_0(\boldsymbol{\theta_n})$ is a prior chosen for each parameter in the MCMC fit. Uniform priors are chosen for all parameters but the LD coefficients and orbital eccentricity (Section 2). From this point, individual planet properties need to be recast within a population-level joint posterior probability depending on the hyperparameters $\boldsymbol{\alpha}$:

$$p\left(\{\boldsymbol{\theta_n}\}, \boldsymbol{\alpha} \mid \{\boldsymbol{y_n}\}\right) \propto p\left(\{\boldsymbol{y_n}\} \mid \{\boldsymbol{\theta_n}\}\right) p\left(\{\boldsymbol{\theta_n}\} \mid \boldsymbol{\alpha}\right) p\left(\boldsymbol{\alpha}\right). \quad (4)$$

This relies on the fact that the global PPD, likelihood, and prior for all parameters are the product of individual PPD, likelihoods, and priors, respectively.

Since the goal is to constrain the population-level model parameters $\boldsymbol{\alpha}$, individual planetary parameters in Equation (4) need to be marginalized to obtain the likelihood of $\boldsymbol{\alpha}$:

$$\mathcal{L}_{\boldsymbol{\alpha}} = \prod_{n=0}^{N} \int d\boldsymbol{\theta_n} p(\boldsymbol{y_n} \mid \boldsymbol{\theta_n}) p(\boldsymbol{\theta_n} \mid \boldsymbol{\alpha}), \quad (5)$$

which can be approximated as

$$\mathcal{L}_{\boldsymbol{\alpha}} \approx \prod_{n=0}^{N} \frac{1}{K} \sum_{k=0}^{K} \frac{p(\boldsymbol{\theta_{nk}} \mid \boldsymbol{\alpha})}{p_0(\boldsymbol{\theta_{nk}})} \quad (6)$$

with

$$p(\boldsymbol{\theta_{nk}} \mid \boldsymbol{\alpha}) \equiv \frac{f_{\boldsymbol{\alpha}}(\psi_{nk}) p_0(\boldsymbol{\theta_{nk}})}{p_0(\psi_{nk})}, \quad (7)$$

where K is the number of samples in the PPD. This is a marginal likelihood where nuisance parameters are now under the form of priors. ψ_{nk} is the population-level distribution that is searched for.

3.2. Dependence of T_B with the Stellar Incident Flux

I now tailor the general framework described above to investigate the dependence of the brightness temperature excess, $\Delta T = T_B - T_{\rm eq,max}$, with equilibrium temperature, $T_{\rm eq,max}$. I use a simple parameterized model to describe the intrinsic distribution of ΔT that depends on $\boldsymbol{\alpha}$:

$$f_{\boldsymbol{\alpha}}(\Delta T_{nk}) = \gamma T_{\rm eq,max,nk} + \zeta \quad (8)$$

with $\boldsymbol{\alpha} \equiv (\gamma, \zeta)$ and adopting uniform priors on γ and ζ. I use the ΔT PPD extracted from the MCMC as inputs by truncating the lower end of the T_B distribution to $T_{\rm eq,0}$. In other words, I hypothesize for each planet that T_B cannot be below $T_{\rm eq,0}$.

I find a median value of $\gamma = -0.32^{+0.26}_{-0.24}$. Based on the current data, the ΔT versus $T_{\rm eq,0}$ trend is thus not robustly detected. As previously discussed, this could be due to the fact that a small ΔT is easier to characterize in the high-irradiation regime. The upper envelope of Figure 3 represents a subset of the super-Earth population that exhibits large ΔT but is not representative of the whole population of super-Earths studied here.

3.3. Determination of a Population Level, A_g

I use the same model as Equation 8 to infer the geometric albedo in the *Kepler* bandpass, A_g. The "total albedo" A_t is distinguished from $A_{g,\rm min}$ as well as $A_{g,\rm max}$, which correspond to minimum and maximum albedo estimates after decontamination from $T_{\rm eq,max}$ and $T_{\rm eq,0}$, respectively (Heng & Demory 2013). I find median $A_t = 0.32$, $A_{g,\rm max} = 0.30$ (95% upper limit of 0.56), and $A_{g,\rm min} = 0.16$ (95% upper limit of 0.47).

4. DISCUSSION

4.1. Comparison With Published Hot Jupiters

I base this comparison sample on the hot Jupiters whose albedo and brightness temperature have been published in Heng & Demory (2013), shown as triangles on Figure 2. These planets are TrES-2b, Kepler-5b, Kepler-6b, Kepler-7b, Kepler-8b, Kepler-12b, Kepler-14b, Kepler-15b, Kepler-17b, Kepler-41b, and HAT-P-7b. Most giant planets have brightness temperatures within ~300 K of their maximum equilibrium temperature. Super-Earth exoplanets discussed in this Letter have larger scatter and they exhibit brightness temperature excesses up to ~1000 K. Figure 3 shows that hot Jupiters generally match a decreasing trend toward a null excess, as shown for HAT-P-7b (Pal et al. 2008), which is the archetype of highly irradiated, low-albedo hot Jupiters with a very low heat recirculation efficiency (Christiansen et al. 2010; Spiegel & Burrows 2010). There are also hot Jupiters having negligible T_B excesses, owing to their low albedos such as TrES-2b (e.g., Barclay et al. 2012). Kepler-7b appears as an outlier in this figure because of its large albedo (Demory et al. 2013).

I find minimum and maximum geometric albedos for hot Jupiters of $A_{g,\rm min} = 0.06 \pm 0.08$ and $A_{g,\rm max} = 0.11 \pm 0.09$, respectively, which are statistically smaller than geometric albedos found for super-Earths.

4.2. Close-in Super-Earth Properties

Close-in super-Earths ($1.0 < R_P < 2.25\ R_\oplus$) have geometric albedos spanning a large range of values in the *Kepler* bandpass. I find that 21 out of the 27 candidates have radii $R_P \leqslant 1.6\ R_\oplus$, suggesting that most of the targets are likely rocky (Lopez & Fortney 2013; Rogers 2014). For larger, strongly irradiated planets such as 55Cnc e, one could not discard the possibility that a significant brightness temperature excesses in the visible (see Cowan & Agol 2011) could be due to the fact that the *Kepler* bandpass probes the deep layers of an envelope of volatiles such as water. In such a case, the incident heat recirculation across longitude at high pressure is more efficient, but a strong greenhouse effect would dramatically increase the brightness temperature. In the case of the close-in super-Earths that are part of this work, I argue that the source of reflected light may originate from (1) the surface, (2) Rayleigh scattering in an atmosphere that may have absorbers in the visible (Na and K), or (3) reflective clouds.

4.2.1. Atmospheres

The range of geometric albedos that are observed for close-in super-Earths suggests that strong alkali metal absorption in the visible is not as generalized as it is for hot Jupiters. The objects forming the upper envelope of brightness temperature excesses (Figure 3) may provide information about the incidence of stellar irradiation on atmospheric visible absorption. Above $T_{\rm eq,0} \sim$ 2200 K, the observed brightness temperature can be explained by thermal emission alone. One possible explanation is that at these high temperatures, the column density of atmospheric constituents may be higher because of the increased evaporation rate of the planet surface (Miguel et al. 2011). Such high-pressure atmosphere would have a higher concentration of alkali metals that would result in an increased absorption at visible wavelengths, hence a lower albedo. At cooler temperatures, the lower evaporation rate would yield an atmosphere with a lower opacity at visible wavelengths. Those super-Earths that have a constraint on the occultation depth extend to moderate equilibrium temperatures ($T_{\rm eq,0} \sim$ 1200 K). In this irradiation regime, particles could condense in the atmosphere, resulting in the possible formation of reflective clouds (Schaefer & Fegley 2009). Constraining the dependence of brightness temperature excesses with stellar incident flux using a larger sample of objects will be key to constrain atmospheric chemistry and dynamics on super-Earths.

4.2.2. Surfaces

It has been shown for Kepler-10b (Batalha et al. 2011) that a lava-ocean model yields very low incident radiation absorption and strong back-scattering by molten lava, resulting in a large albedo, $A_g \sim 0.4$ (Rouan et al. 2011). I find similarly large albedos for a subset of the super-Earths studied here. Still considering Kepler-10b, a wide range of solid surface compositions (Hu et al. 2012) could match the observed excess of brightness temperature in the *Kepler* bandpass. Determining how mineral reflective properties evolve through molten phases with increasing temperature will be paramount to lift this degeneracy.

Those super-Earths that have large geometric albedos represent promising targets for their characterization using future facilities operating in the visible such as CHEOPS (Broeg et al. 2013) and the High Resolution Spectrograph (HIRES) that will be installed on the E-ELT (Maiolino et al. 2013)

using spectroscopic direct detection (Martins et al. 2013). New occultation follow-up studies of a well defined sample of strongly irradiated super-Earths will have the ability to constrain the range of plausible surface compositions of these exoplanets by improving the precision on planetary emission at visible and infrared wavelengths. Treating a population of planets as a whole to search for common trends may turn out to be a complementary approach to firmly constrain the surface/atmosphere properties of the ubiquitous small exoplanets.

The author thanks Julien de Wit, Farhan Feroz, Michael Gillon, Kevin Heng, Renyu Hu, Nikku Madhusudhan, Leslie Rogers, Roberto Sanchis-Ojeda, Sara Seager, Vlada Stamenkovic, and Andras Zsom for providing comments that improved the manuscript. The author also thanks the anonymous referee for a very helpful review. The author gratefully acknowledges the *Kepler* team for generating and vetting the *Kepler* data sets. This research made use of the IDL Astronomical Library and the IDL-Coyote Graphics Library.

Facility: Kepler

REFERENCES

Barclay, T., Huber, D., Rowe, J. F., et al. 2012, ApJ, 761, 53
Batalha, N. M., Borucki, W. J., Bryson, S. T., et al. 2011, ApJ, 729, 27
Batalha, N. M., Rowe, J. F., Gilliland, R. L., et al. 2010, ApJL, 713, L103
Broeg, C., Fortier, A., Ehrenreich, D., et al. 2013, in Hot Planets and Cool Stars European Physical Journal Web of Conferences, Vol. 47, ed. R. Saglia (Les Ulis, France: EDP Sciences), 3005
Burke, C. J., Bryson, S. T., Mullally, F., et al. 2014, ApJS, 210, 19
Castan, T., & Menou, K. 2011, ApJL, 743, L36
Charbonneau, D., Berta, Z. K., Irwin, J., et al. 2009, Natur, 462, 891
Christiansen, J. L., Ballard, S., Charbonneau, D., et al. 2010, ApJ, 710, 97
Claret, A., & Bloemen, S. 2011, A&A, 529, 75
Cowan, N. B., & Agol, E. 2011, ApJ, 729, 54
Deming, D., & Seager, S. 2009, Natur, 462, 301
Demory, B.-O., de Wit, J., Lewis, N., et al. 2013, ApJL, 776, L25
Demory, B.-O., Gillon, M., Deming, D., et al. 2011, A&A, 533, 114
Demory, B.-O., & Seager, S. 2011, ApJS, 197, 12
Dragomir, D., Matthews, J. M., Eastman, J. D., et al. 2013, arXiv:1305.7260
Fressin, F., Torres, G., Charbonneau, D., et al. 2013, ApJ, 766, 81
Gelman, & Rubin. 1992, StaSc, 7, 457
Gillon, M., Lanotte, A. A., Barman, T., et al. 2010, A&A, 511, 3
Gillon, M., Triaud, A. H. M. J., Fortney, J. J., et al. 2012, A&A, 542, A4
Gustafsson, B., Edvardsson, B., Eriksson, K., et al. 2008, A&A, 486, 951
Hadden, S., & Lithwick, Y. 2014, ApJ, 787, 80
Hansen, B. M. S. 2008, ApJS, 179, 484
Heng, K., & Demory, B.-O. 2013, ApJ, 777, 100
Heng, K., & Kopparla, P. 2012, ApJ, 754, 60
Hogg, D. W., Myers, A. D., & Bovy, J. 2010, ApJ, 725, 2166
Hu, R., Ehlmann, B. L., & Seager, S. 2012, ApJ, 752, 7
Huber, D., Silva Aguirre, V., Matthews, J. M., et al. 2014, ApJS, 211, 2
Jenkins, J. M., Caldwell, D. A., Chandrasekaran, H., et al. 2010, ApJL, 713, L120
Kipping, D. M. 2010, MNRAS, 408, 1753
Léger, A., Rouan, D., Schneider, J., et al. 2009, A&A, 506, 287
Lopez, E. D., & Fortney, J. J. 2013, arXiv:1311.0329
Maiolino, R., Haehnelt, M., Murphy, M. T., et al. 2013, arXiv:1310.3163
Martins, J. H. C., Figueira, P., Santos, N. C., & Lovis, C. 2013, MNRAS, 436, 1215
Miguel, Y., Kaltenegger, L., Fegley, B., & Schaefer, L. 2011, ApJL, 742, L19
Miller-Ricci, E., & Fortney, J. J. 2010, ApJL, 716, L74
Ofir, A., & Dreizler, S. 2013, A&A, 555, A58
Pal, A., Bakos, G. A., Torres, G., et al. 2008, ApJ, 680, 1450
Rogers, L. A. 2014, ApJ, submitted
Rogers, L. A., & Seager, S. 2010, ApJ, 716, 1208
Rouan, D., Deeg, H. J., Demangeon, O., et al. 2011, ApJL, 741, L30
Sanchis-Ojeda, R., Rappaport, S., Winn, J. N., et al. 2013, ApJ, 774, 54
Schaefer, L., & Fegley, B. 2009, ApJL, 703, L113
Slawson, R. W., Prša, A., Welsh, W. F., et al. 2011, AJ, 142, 160
Spiegel, D. S., & Burrows, A. 2010, ApJ, 722, 871
Still, M., & Barclay, T. 2012, PyKE: Reduction and analysis of Kepler Simple Aperture Photometry Data, Astrophysics Source Code Library
Winn, J. N., Matthews, J. M., Dawson, R. I., et al. 2011, ApJL, 737, L18